

See discussions, stats, and author profiles for this publication at: <https://www.researchgate.net/publication/280870371>

# Controllable Grain Morphology of Perovskite Absorber Film by Molecular Self-Assembly toward Efficient Solar Cell Exceeding 17%

ARTICLE in JOURNAL OF THE AMERICAN CHEMICAL SOCIETY · AUGUST 2015

Impact Factor: 12.11 · DOI: 10.1021/jacs.5b06444 · Source: PubMed

---

READS

110

5 AUTHORS, INCLUDING:



Wenzhe Li

Tsinghua University

17 PUBLICATIONS 231 CITATIONS

SEE PROFILE



Jiangwei Li

Tsinghua University

5 PUBLICATIONS 31 CITATIONS

SEE PROFILE



Yaohua Mai

Hebei University

55 PUBLICATIONS 397 CITATIONS

SEE PROFILE



Liduo Wang

Tsinghua University

213 PUBLICATIONS 4,133 CITATIONS

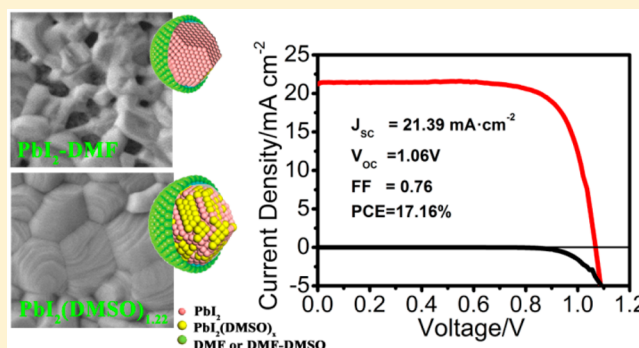
SEE PROFILE

## Controllable Grain Morphology of Perovskite Absorber Film by Molecular Self-Assembly toward Efficient Solar Cell Exceeding 17%

Wenzhe Li,<sup>†</sup> Jiandong Fan,<sup>\*,‡</sup> Jiangwei Li,<sup>†</sup> Yaohua Mai,<sup>‡</sup> and Liduo Wang<sup>\*,†</sup><sup>†</sup>Key Lab of Organic Optoelectronics & Molecular Engineering of Ministry of Education, Department of Chemistry, Tsinghua University, Beijing 100084, China<sup>‡</sup>College of Physics Science and Technology, Hebei University, Baoding, 071002, China

## Supporting Information

**ABSTRACT:** The highly developed crystallization process with respect to perovskite thin films is favorable for efficient solar cells. Here, an innovative intermolecular self-assembly approach was employed to retard the crystallization of PbI<sub>2</sub> in dimethylformamide (DMF) by additional solvent of dimethyl sulfoxide (DMSO), which was proved to be capable of coordinating with PbI<sub>2</sub> by coordinate covalent bond. The obtained PbI<sub>2</sub>(DMSO)<sub>x</sub> (0 ≤ x ≤ 1.86) complexes tend to be closely packed by means of intermolecular self-assembly. Afterward, an intramolecular exchange of DMSO with CH<sub>3</sub>NH<sub>3</sub>I (MAI) enabled the complexes to deform their shape and finally to reorganize to be an ultraflat and dense thin film of CH<sub>3</sub>NH<sub>3</sub>PbI<sub>3</sub>. The controllable grain morphology of perovskite thin film allows obtaining a power conversion efficiency (PCE) above 17% and a stabilized power output above 16% within 240 s by controlling DMSO species in the complex–precursor system (CPS). The present study gives a reproductive and facile strategy toward high quality of perovskite thin films and efficient solar cells.



## INTRODUCTION

Since the first attempt to use CH<sub>3</sub>NH<sub>3</sub>PbI<sub>3</sub>/CH<sub>3</sub>NH<sub>3</sub>PbBr<sub>3</sub> as a semiconductor in a solar cell was undertaken,<sup>1</sup> inorganic–organic perovskite-based solar cells have attracted intensive attention, which boost the power conversion efficiencies (PCE) from 3.8% in 2009 to a recent 20.1%.<sup>2–11</sup> As light-absorber film, the perovskite materials have demonstrated excellent photovoltaic performance, i.e., large absorption coefficient, high carrier mobility, long carrier diffusion, and direct band gap.<sup>12–14</sup> A highly crystallized perovskite thin film without defect is likely to be the main segment that gives rise to a solar cell with satisfactory photovoltaic property. The perovskite layers with a well-defined grain structure, full surface coverage, and small surface roughness allow realization of an efficient solar cell.<sup>15–18</sup> Various methods including solution-based techniques,<sup>19,20</sup> low-temperature vapor-assisted solution process,<sup>21–23</sup> and vacuum-evaporation deposition<sup>5,18</sup> were employed to prepare the perovskite thin film. Among them, a two-step solution-process deposition technique was demonstrated to be particularly useful for preparing films of organic–inorganic systems, in which the organic component is difficult to evaporate, and/or for systems in which the inorganic and organic components have incompatible solubility characteristics. This technique was largely successful in the preparation of perovskite films especially for those with nanostructured TiO<sub>2</sub> scaffolds and greatly increased the reproducibility of the cell performance. However, the two-step solution process often results in films

with significantly large surface roughness that was frequently peeled off from the substrate.<sup>24–27</sup> To solve it, a strongly coordinative solvent of dimethyl sulfoxide (DMSO) was introduced into the  $\gamma$ -butyrolactone precursor solution of CH<sub>3</sub>NH<sub>3</sub>I(MAI), CH<sub>3</sub>NH<sub>3</sub>Br(MABr), NH<sub>2</sub>CH=NH<sub>2</sub>I(FAI), and NH<sub>2</sub>CH<sub>2</sub>NH<sub>2</sub>Br(FABr) powders with PbI<sub>2</sub> and PbBr<sub>2</sub> with an aim of forming the different iodide and/or bromide complexes, which facilitated to improve the dissolubility and form dense perovskite films.<sup>4</sup> Later on, strong coordinative DMSO instead of dimethylformamide (DMF) as the solvent for PbI<sub>2</sub> retarded the crystallization of PbI<sub>2</sub> and resulted in extremely uniform perovskite films by a two-step sequential deposition.<sup>28</sup> Very recently, a sequential reaction approach toward depositing high-quality FAPbI<sub>3</sub> films involved FAPbI<sub>3</sub> crystallization by means of a direct intramolecular exchange of dimethyl sulfoxide (DMSO) molecules intercalated in PbI<sub>2</sub> with FAI. The champion cell with over 20% efficiency was obtained by this technique.<sup>9</sup> All of these studies mentioned above clearly indicate that DMSO has a strong coordination ability with PbI<sub>2</sub> by which the strong interaction between DMSO and Pb<sup>2+</sup> can retard the crystallization of PbI<sub>2</sub>. In this scenario, the introduction of DMSO would be favorable to the crystallization of perovskite thin films. Importantly, the trade-off between DMF and DMSO as solvents in the precursor solution is

Received: June 22, 2015

Published: August 6, 2015

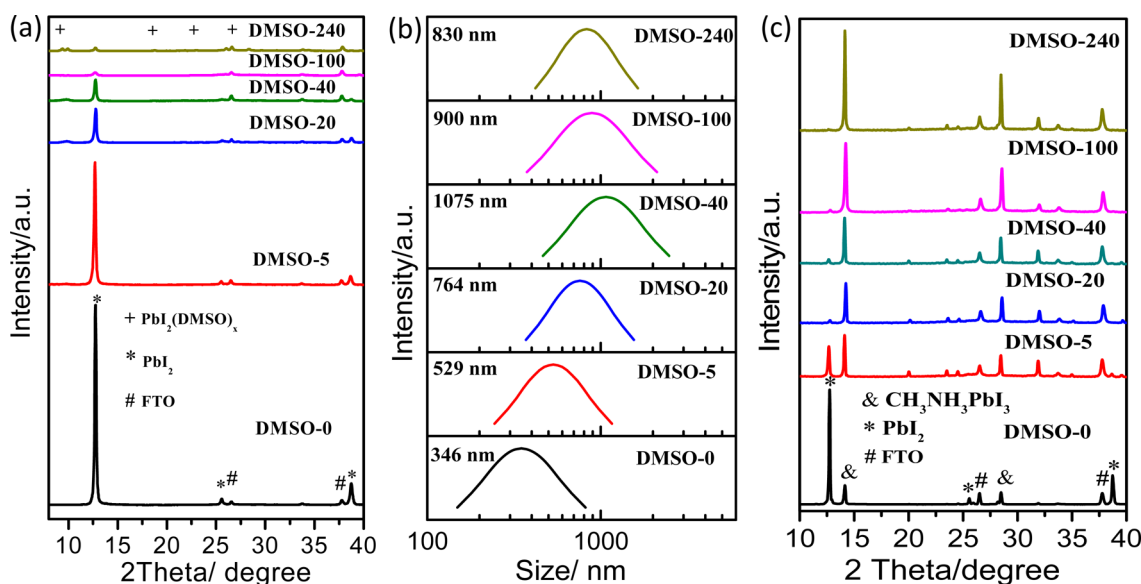


**Figure 1.** (a) XRD patterns of  $\text{PbI}_2(\text{DMSO})_x$  ( $0 \leq x \leq 1.86$ ) complexes. (b) Size distributions of  $\text{PbI}_2(\text{DMSO})_x$  complexes in CPS detected by dynamic light scattering. (c) XRD patterns of  $\text{CH}_3\text{NH}_3\text{PbI}_3$  perovskite thin films.

supposed to control the crystallization of perovskite thin film, further enhancing the photovoltaic performances of solar cells. Nevertheless, the existing techniques suffer from either complicated procedure to prepare  $\text{PbI}_2$ –DMSO complex or uncontrollable ratio of  $\text{PbI}_2$  and DMSO that has a significant effect on tuning the grain size of perovskite layers.<sup>4,9,28,29</sup>

In the present study, we found that the controlled ratio of DMF and DMSO in the complex–precursor system (CPS) can bring about a series  $\text{PbI}_2(\text{DMSO})_x$  ( $0 \leq x \leq 1.86$ ) complexes. The formed  $\text{PbI}_2$ –DMSO complexes with different  $x$  value in  $\text{PbI}_2(\text{DMSO})_x$  in turn effectively control the grain morphology, density, and roughness of perovskite thin film. By molecular self-assembly approach, the as-prepared mirror-like perovskite thin films allow obtaining an efficient and stable solar cell. Likewise, a potential mechanism concerning the perovskite crystal growth by molecular self-assembly approach in the presence of DMSO complex was presented in view of microscopic dynamics.

## RESULTS AND DISCUSSIONS

Here, we have systematically explored the effects of the given ratio in a quantity between DMSO and DMF on the crystallization quality, film morphology, and photovoltaic performance. In order to clarify the ratio of DMSO and DMF in CPS, we named DMSO-0, DMSO-5, DMSO-20, DMSO-40, DMSO-100, and DMSO-240 in the following discussions, and the numbers represent the particular volume of DMSO in the mixed solvent of 240  $\mu\text{L}$ .

In the present study, a two-step sequential deposition method was employed to prepare the perovskite thin film. First of all, we studied the influence of DMSO on the  $\text{PbI}_2$  thin film with respect to its stronger coordination ability with  $\text{PbI}_2$  in comparison to DMF. Figure 1a displays the evolution of the XRD patterns of  $\text{PbI}_2$  thin film with DMSO ratio increasing. In the case of DMSO-0, the XRD patterns are exactly consistent with  $\text{PbI}_2$  peaks at  $12.6^\circ$  and  $38.0^\circ$ .<sup>30</sup> With the DMSO ratio increasing from 8.3% (DMSO-20) to 16.7% (DMSO-40), the intensities of  $\text{PbI}_2$  diffraction peaks are obviously quenched, whereas the peaks that are associated with  $\text{PbI}_2(\text{DMSO})_x$

complex tend to appear, which suggests that the presence of DMSO retards the crystal growth of  $\text{PbI}_2$  along all of the crystallographic directions during the formation of  $\text{PbI}_2(\text{DMSO})_x$  complex. When the case moves to DMSO-240, all of the diffraction peaks at  $9.9^\circ$  and  $26.0^\circ$  contributed to the  $\text{PbI}_2(\text{DMSO})_2$  complex,<sup>9</sup> which confirms the formation of  $\text{PbI}_2(\text{DMSO})_2$  in the presence of DMSO instead of DMF.

The size distributions of  $\text{PbI}_2(\text{DMSO})_x$  complexes were tested by zeta potential analyzer (Figure 1b). The average size of  $\text{PbI}_2$  powder dissolved in pure DMF solvent was detected to be 346 nm. Afterward, the complex grew larger with the introduction of more DMSO. Unexpectedly, the average size of as-prepared complex in the case of DMSO-40 was 1075 nm, which is the biggest one among all cases. And then the average size decreased to 830 nm, when  $\text{PbI}_2$  dissolved in pure DMSO solvent. A likely explanation concerning the size distributions will be given later. The top–down morphology of the corresponding film was separately observed by SEM (Figure S1). In the case of pure DMF, it appeared that the highly crystallized  $\text{PbI}_2$  grew along one direction, which led to a lower surface coverage as shown in the ref 28. In the presence of DMSO, the surface coverage has a clear improvement and the morphology of  $\text{PbI}_2(\text{DMSO})_x$  complex was changed from arborization to sphere. Meanwhile, we found that its size was linearly growing with the concentration of DMSO. Once again, the size of complex (242 nm) was identified to be the biggest one in the case of DMSO-40. After that, a lot of pinholes were found on the surface when the concentration of DMSO kept increasing. Clearly, the morphology evolution of  $\text{PbI}_2(\text{DMSO})_x$  thin film is consistent with the size distributions when it dissolved in the solvent.

Figure 2 demonstrates the evolution of the absorbance of  $\text{PbI}_2(\text{DMSO})_x$  complex. In the case of DMSO-0, the absorption band-edge located at round 525 nm is associated with the band-gap excitation of crystallized  $\text{PbI}_2$  thin film,<sup>31</sup> which certifies that the process of  $\text{PbI}_2$  crystal growth has been preliminarily finalized during the first-step spin coating. With the introduction of DMSO in CPS, the absorption band-edge shifts toward the ultraviolet direction until it finally disappears in the case of DMSO-240. It turns out that the as-prepared thin

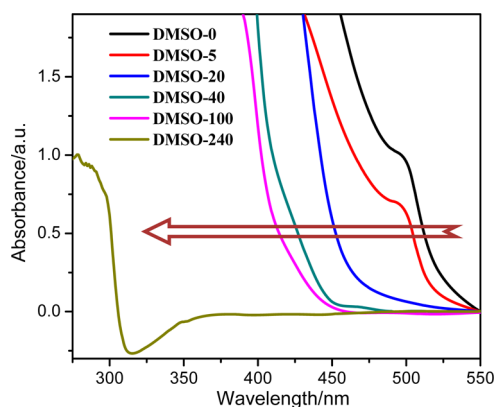


**Figure 2.** UV-vis absorption spectra of  $\text{PbI}_2(\text{DMSO})_x$  ( $0 \leq x \leq 1.86$ ) complexes.

films of  $\text{PbI}_2(\text{DMSO})_x$  complex tend to be amorphous, which was also concluded from XRD patterns in which the intensity of diffraction peaks was quenched step by step in the presence of DMSO.

XPS was used to further certify the existence of the  $\text{PbI}_2(\text{DMSO})_x$  complex. Figure 3 displays the XPS of as-prepared  $\text{PbI}_2(\text{DMSO})_x$  thin films. As shown in Figure 3a, the main peaks at 138.5 eV were ascribed to the binding energy of Pb–I. The fitting peaks situated at 137.0 eV were identified as the binding energy of Pb–O, which was considered as the bridge connecting  $\text{PbI}_2$  and DMSO. As expected, we did not detect such a peak in the case of DMSO-0. Nonetheless, this peak appeared in the case of DMSO-40, and its intensity strengthened when the DMF solvent was completely replaced by the DMSO solvent, which indicated that more  $\text{PbI}_2(\text{DMSO})_x$  complexes were formed with more DMSO involved in CPS. Herein, the  $x$  values were calculated to be 0 (DMSO-0), 0.92 (DMSO-20), 1.22 (DMSO-40), 1.57 (DMSO-100), and 1.86 (DMSO-240), respectively. It should be noted that we found a peak that was positioned at around 139.5 eV for all of these three cases, which were likely to be associated with the oxidation of  $\text{PbI}_2$ . Likewise, the spectrum of O 1s was also detected with the exact same sample (Figure 3b). Different from DMSO-0, the peaks that were ascribed to the band of S–O in DMSO were found by fitting the spectra of DMSO-40 and DMSO-240, respectively. Unlike DMSO-0, the

detected peaks that were located at 529.5 eV in the cases of DMSO-40 and DMSO-240 were identified as the oxygen in  $\text{PbO}_2$ . The fit peaks of metal oxide further confirmed the formation of  $\text{PbI}_2(\text{DMSO})_x$ . Again, in comparison to DMSO-40, the enhanced intensity suggested that more DMSO molecules were coordinated with  $\text{PbI}_2$  in the case of DMSO-240. All of these results provided the possibility of controlling the  $x$  value in the range of 0–1.86 while tuning the ratio of DMSO and DMF in CPS.

As previously reported,<sup>32</sup> in the presence of pure DMF as solvent, DMF molecule was proved to be coordinated to Pb to form one-dimensional structures of  $\text{PbI}_2 \cdot \text{DMF}$  along the  $a$  axis. The formation of a Pb–O coordination bond implied the possibility of attractive interactions between Pb and oxygen. Meanwhile, the  $\text{PbI}_2(\text{DMSO})_2$  complex was synthesized by a solution-processed approach at room temperature<sup>33</sup> and its crystal structure was solved by the heavy-atom method that refined the positional and anisotropic thermal parameters for non-hydrogen atoms by the block-diagonal least-squares method.<sup>34</sup> The space group was assumed to be  $C_{mmm}$ , which is completely different from  $\text{PbI}_2$  crystal. In the structure of  $\text{PbI}_2(\text{DMSO})_2$  complex, the crystal has skeletal linear chain structure consisting of  $[\text{Pb} < \frac{I}{I} >]_n$ , two DMSO molecules coordinate to the Pb atom through their O atoms in trans position, and the direction of the Pb–O bond formation is indeterminate. In the mixed system of DMSO and DMF,  $\text{PbI}_2$  prefers to coordinate with DMSO, since the DMSO has a stronger coordination ability with  $\text{PbI}_2$  than that of DMF.<sup>28</sup> Consequently, the as-formed  $\text{PbI}_2(\text{DMSO})_x$  complexes would homogeneously distribute into the DMF solvent. With the ratio of DMSO increasing in CPS, the coordinated DMSO in the complex would favor assembly of the  $\text{PbI}_2$  somehow. The as-formed “micella” may contribute to the increased size as certified in Figure 1b and Figure S2. When the concentration of DMSO exceeded a value (DMSO-100), it caused an accumulation of  $\text{PbI}_2(\text{DMSO})_x$  complexes in CPS, hence forming a macroscopic needle-shaped crystal, which gave rise to a reduced concentration of  $\text{PbI}_2(\text{DMSO})_x$  complex. These explanations could elucidate the decreased average size and lower coverage as shown in Figure 1b and Figure S1 when the concentration of DMSO exceeded a value (DMSO-100). It is well-known that DMF is of great benefit to the growth of  $\text{PbI}_2$

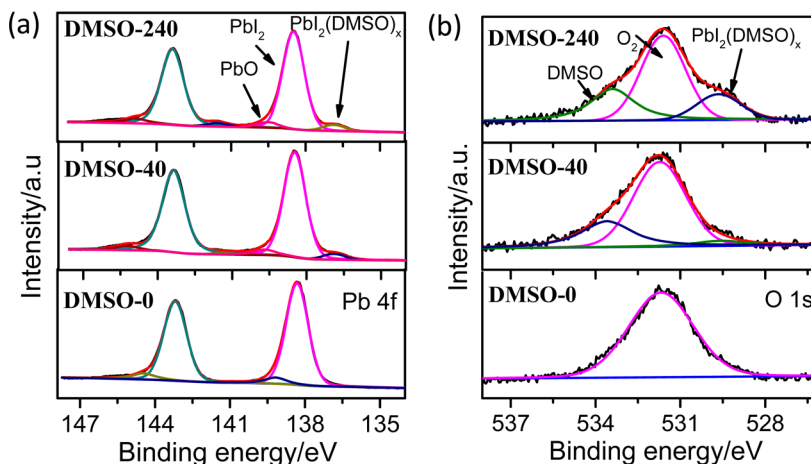


**Figure 3.** High-resolution XPS of  $\text{PbI}_2(\text{DMSO})_x$  ( $0 \leq x \leq 1.86$ ) complexes thin film prepared in the concentration of DMSO-0, DMSO-40, and DMSO-240: (a) spectra of Pb  $4f_{7/2}$  and Pb  $4f_{5/2}$ ; (b) spectra of O  $1s$ .



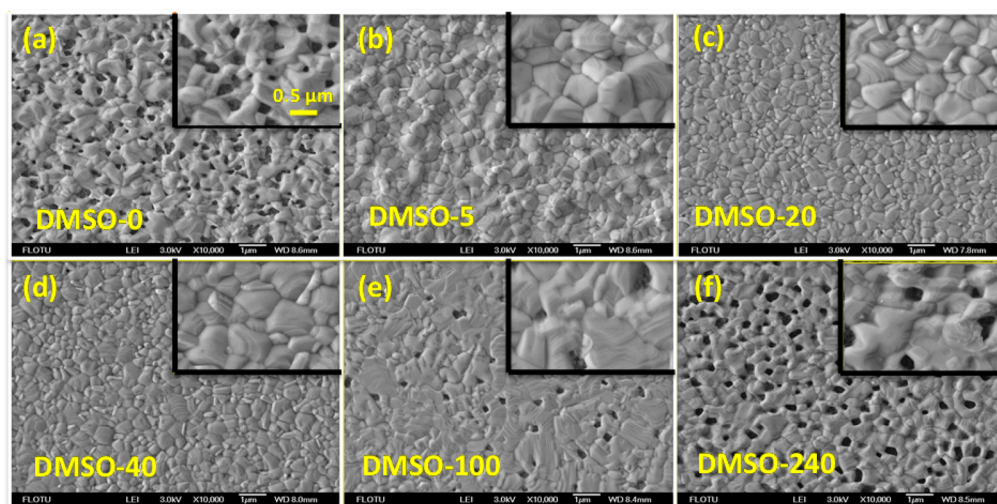


**Figure 4.** Top-down SEM images of perovskite thin films prepared by different ratios of DMSO and DMF in CPS. Insets are the corresponding details of the images with lower magnification. (a) DMSO-0; (b) DMSO-5; (c) DMSO-20; (d) DMSO-40; (e) DMSO-100; (f) DMSO-240.

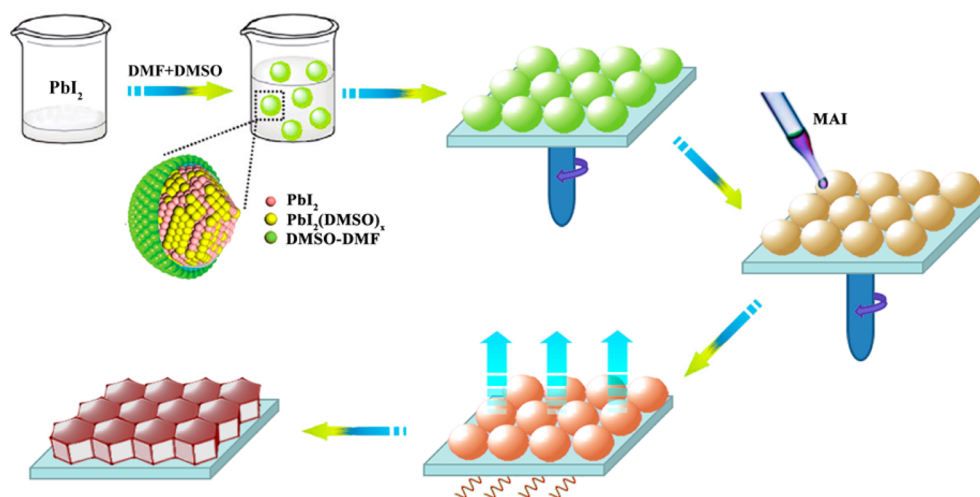


**Figure 5.** Schematic view of the crystal growth process of perovskite thin film via molecular self-assembly approach in the presence of DMSO.

crystal, whereas the DMSO retards the crystallization of  $\text{PbI}_2$ .<sup>28</sup> Herein, a certain amount of DMF involved in CPS is favorable to dissolve/disperse the as-formed  $\text{PbI}_2(\text{DMSO})_x$  complexes, which enables the CPS to be stable. In particular, in the case of DMSO-40, i.e., DMF is 200  $\mu\text{L}$  in CPS, the precursor solution is able to remain stable for a couple of months. Again, the  $\text{PbI}_2(\text{DMSO})_2$  crystal will be obtained in a few hours in the presence of pure DMSO as solvent in CPS as previously mentioned.

To further figure out the influence of DMSO on the crystallization of  $\text{CH}_3\text{NH}_3\text{PbI}_3$ , we have carried out the XRD of as-prepared  $\text{CH}_3\text{NH}_3\text{PbI}_3$  with different DMSO ratios in CPS. As shown in Figure 1c, the intensity of the peak located at  $12.6^\circ$  that is associated with  $\text{PbI}_2$  continues to decrease while the peaks that are ascribed to  $\text{CH}_3\text{NH}_3\text{PbI}_3$  become stronger with the DMSO ratio increasing. The opposite evolutions between  $\text{PbI}_2$  and perovskite suggest that the DMSO and/or  $\text{PbI}_2(\text{DMSO})_x$  complex aids the crystal growth of perovskite thin film along all of the crystallographic directions.

Figure 4 exhibits the top-down SEM images of perovskite thin films prepared by tuning the DMSO concentration in the CPS, which clearly displays their different grain size, surface

roughness, and coverage. We found that the grain size and coverage of the films are consistent with the size distribution of  $\text{PbI}_2(\text{DMSO})_x$  complex in CPS. Besides, the topographical images of the as-prepared  $\text{CH}_3\text{NH}_3\text{PbI}_3$  film were measured under ambient air with an atom force microscope (Figure S3). Again, the root mean square (RMS) of film by DMSO-40 was demonstrated to be only 26 nm, which is much lower than that by DMSO-0 (63.7 nm) and DMSO-240 (61.8 nm). Such phenomenon implies that the introduction of DMSO played a crucial role in the process of the nucleation and crystallization of  $\text{PbI}_2$  and  $\text{CH}_3\text{NH}_3\text{PbI}_3$  thin film.

Herein, we proposed a potential mechanism concerning the perovskite crystal growth by molecular self-assembly in the presence of DMSO complex in view of microscopic dynamics as shown in Figure 5. In the first stage, the DMSO molecules intercalated in  $\text{PbI}_2$  once the  $\text{PbI}_2$  powder dissolved in DMSO, which results in the formation of  $\text{PbI}_2(\text{DMSO})_x$  ( $0 \leq x \leq 1.86$ ) complex. Second, the concentration and contact of the as-prepared  $\text{PbI}_2(\text{DMSO})_x$  complex will follow up with the evaporation of solvent as shown in Figure 5. During the process, the DMSO species are advantageous to the development of amorphous mirror-like film as shown in Figure S1b–d.

Clearly, the  $\text{PbI}_2(\text{DMSO})_x$  complexes are proposed to arrange in an orderly way by molecular self-assembly as shown in Figure 5. Comparatively, in the case of DMSO-0, the highly crystallized  $\text{PbI}_2$  film leads to a  $\text{CH}_3\text{NH}_3\text{PbI}_3$  film with significant roughness and pinholes as shown in Figure S1a. Third, the DMSO will be exchanged by MAI because of its smaller affinity toward  $\text{PbI}_2$  compared to MAI, which enables the complexes to deform their shape (Figure S1 and Figure 4). The deformation occurs because the capillary and osmotic pressures are able to overcome the internal stresses in the system.<sup>35</sup> In this scenario, the  $x$  value is apparently essential for highly dense and fully covered film with respect to the exchange of DMSO and MAI. Either excess of DMSO or DMF may give rise to an inhomogeneous film with pinholes as shown in Figure 4a,e,f. In the last stage, the formation of grain boundary is necessary to form a mechanically stable film.

As mentioned above, the intervention of a certain amount of DMSO is beneficial to the formation of perovskite thin films. We studied the photovoltaic performance of perovskite solar cells prepared by tuning the concentration of DMSO and DMF. As shown in Figure 6, the  $V_{\text{OC}}$ ,  $J_{\text{SC}}$ , and FF were

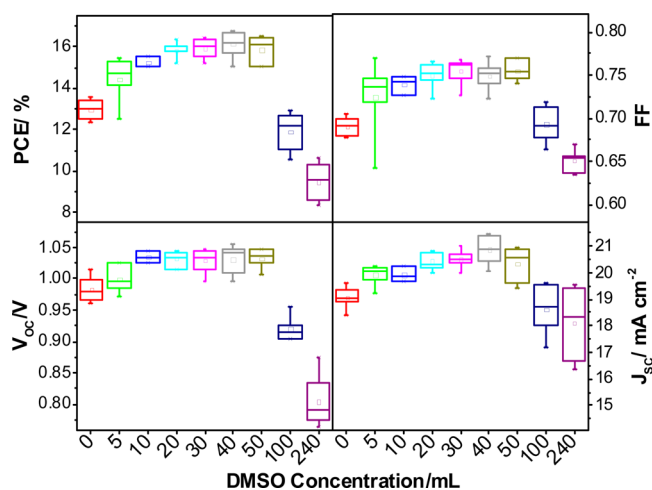


**Figure 6.** Effect of the concentration of DMSO in CPS on the photovoltaic performances of  $\text{CH}_3\text{NH}_3\text{PbI}_3$  solar cell.

enhanced when the concentration varied from DMSO-0 to DMSO-40, which contributed to a substantially improved PCE from 13% to 17%, whereas the photovoltaic performances of the cells were declined when the concentration exceeded

DMSO-40. The PCE was finally decreased to be around 10% when the DMF solvent was completely replaced by DMSO, i.e., the case of DMSO-240. It should be mentioned that the variation of photovoltaic performances is consistent with the size distribution of  $\text{PbI}_2(\text{DMSO})_x$  ( $0 \leq x \leq 1.86$ ) complexes and the morphology evolution of  $\text{CH}_3\text{NH}_3\text{PbI}_3$  thin films, which pointed toward its dynamic mechanism.

Meanwhile, considering the performances of perovskite materials-based solar cells are partly dependent on the concentration of MAI and the thickness of  $\text{TiO}_2$  mesoporous layer, we have explored the effects of these two factors on the photovoltaic performances of the cells (Figures S4 and S5). With the concentration of MAI increasing from 25 to 35 mg/mL, the  $V_{\text{OC}}$  and FF slightly decreased while the  $J_{\text{SC}}$  kept climbing. Consequently, the overall PCE remained stable in this scenario. As for the effect of the thickness of  $\text{TiO}_2$  mesoporous layer, all of the photovoltaic parameters had a similar evolution that were enhanced in the range of 80–150 nm and then shrunk from 150 to 230 nm. Such fluctuation clearly pointed out the optimized vertex that corresponds a 150 nm thickness of a  $\text{TiO}_2$  mesoporous layer. Combining all of the optimized parameters above, we used the  $\text{PbI}_2(\text{DMSO})_{1.22}$  complex as the precursor of  $\text{PbI}_2$  to fabricate a solar cell. Figure 7a gave  $J$ – $V$  curves of the best cell, which exhibited a high  $J_{\text{SC}}$  of 21.39  $\text{mA}/\text{cm}^2$ , a  $V_{\text{OC}}$  of 1.06 V, and a FF of 0.76, resulting in a PCE of 17.16%. The measured  $J_{\text{SC}}$  is consistent with the integrated  $J_{\text{SC}}$  of 19.2  $\text{mA}/\text{cm}^2$  estimated from external quantum efficiency in Figure S6. In order to rule out the influence of hysteresis effects on the transient photocurrent density and stabilized power output of the cells, we performed the photocurrent density and power conversion efficiency as a function of time for the same cell held close to 0.865 V forward bias. As shown in Figure 7b, the photocurrent density and stabilized power output of the cells remained stable within 240 s, and a highly stable PCE over 16% can be obtained. The stable power output efficiency suggests that the present study gives the possibility of an efficient and stable perovskite solar cell prepared by molecular self-assembly.

## CONCLUSIONS

We employed a facile and reproducible approach to obtain a series  $\text{PbI}_2(\text{DMSO})_x$  ( $0 \leq x \leq 1.86$ ) complexes via solution process. The controllable grain size and morphology of  $\text{CH}_3\text{NH}_3\text{PbI}_3$  thin films were obtained by means of molecular self-assembly. The optimized  $\text{PbI}_2(\text{DMSO})_{1.22}$  complex was demonstrated to be favorable to the realization of ultraflat and

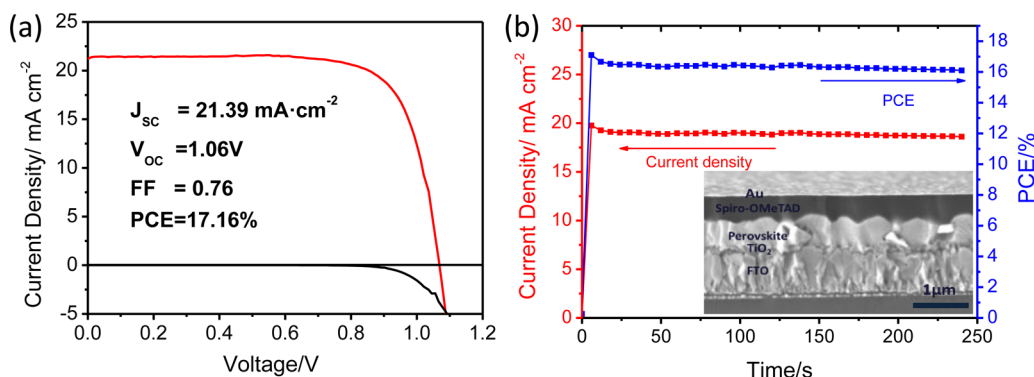


**Figure 7.** (a)  $J$ – $V$  curve of the best performing cell. (b) Photocurrent density and power conversion efficiency as a function of time for the same cell held close to 0.865 V forward bias. Inset is the cross-sectional SEM image of the cell.

superdense film, which allowed fabricating an efficient perovskite solar cell with a PCE of 17.16% and stabilized power output of over 16% within 240 s. The present study provides an effective protocol for fabricating efficient and stable perovskite materials-based solar cell. Further work via molecule assembly approach for improving the efficiency and stability of the cells, e.g., swapping the MAI by FAI that has similar size as DMSO and incorporation of MAPbBr<sub>3</sub> into FAPbI<sub>3</sub>, is underway.

## EXPERIMENTAL SECTION

**Solar Cell Fabrications.** The TiO<sub>2</sub> compact layers were deposited on fluorine-doped tin oxide glass using atomic layer deposition (Beneq TFS 200). In particular, it was prepared at 150 °C in pulse mode with a nitrogen flow of 300 sccm by using titanium tetrachloride (TiCl<sub>4</sub>) and H<sub>2</sub>O as Ti and O precursors, respectively. The TiCl<sub>4</sub> was retained in the chamber for 0.25 s, and subsequently the H<sub>2</sub>O was retained for 0.25 s. The wait period for both precursors was 1 s. At 150 °C, the TiO<sub>2</sub> growth rate per cycle was 0.5 Å, and the TiO<sub>2</sub> deposition was performed for 300 cycles to achieve a layer thickness of 17 nm. The nanocrystalline TiO<sub>2</sub> paste (18NRT from Dyesol Company; diluted to w/w 14.3%) was deposited on the pretreated fluorine-doped tin oxide substrate at 4000 rpm for 30 s, followed by heating at 500 °C for 1 h. The thickness of the annealed TiO<sub>2</sub> films was nearly 150 nm, as determined by scanning electron microscopy (SEM; JEOL JSM-7401F). The 170 mg of PbI<sub>2</sub> (Aldrich, 99.9985%) in 240 μL of DMF (Aldrich, 99.9%) and DMSO (Aldrich, 99.9%) mixed precursor solution was heated at 60 °C for 2 h under magnetic stirring, and the mixture was then spin coated on the as-prepared TiO<sub>2</sub> film at 3000 rpm for 30 s in a glovebox. The films were dropped with a solution of CH<sub>3</sub>NH<sub>3</sub>I in 2-propanol (30 mg/mL) and spin-coated at 5000 rpm for 30 s. Afterward, the as-prepared films were heated at 150 °C for around 20 min until the color changed to dark red. A hole-transporting layer (HTL) was then deposited via spin-coating a 0.8 M solution of 2,2',7,7'-tetrakis(N,N-di-p-methoxyphenylamine) 9,9'-spirobifluorene (spiro-OMeTAD) in chlorobenzene, with additives of lithium bis(trifluoromethanesulfonyl)imide and 4-tert-butylpyridine. Spin-coating was carried out at 2000 rpm for 45 s. Devices were then left overnight in air. Finally, 70 nm gold electrodes were thermally evaporated under vacuum of ~10<sup>-6</sup> Torr, at a rate of ~0.2 nm/s, to complete the device.

**Characterizations.** X-ray diffraction (XRD) patterns were obtained with Smart LAB Instruments Cu Kα beam (λ = 1.54 Å). UV–vis absorption spectra were employed to assess the absorption properties of perovskite sensitized TiO<sub>2</sub> film with a Hitachi U-3010 spectroscope. The morphology of the film was tested with scanning electron microscopy (SEM; JEOL JSM-7401F). The size distributions of PbI<sub>2</sub>(DMSO)<sub>x</sub> complexes in DMF–DMSO mixed solvent were tested by zeta potential analyzer (Brookhaven ZetaPlus). The prepared solutions were filtered by polytetrafluoroethylene (PTFE) (porous size, 220 nm) prior to characterizations. X-ray photoelectron spectroscopy (XPS) was measured with a PHI 5300 ESCA PerkinElmer spectrometer. All spectra were shifted to account for sample charging using inorganic carbon at 284.80 eV as a reference. The topographical and potential phase maps were measured under ambient air with an atom force microscope (Seiko Instruments SPA 400). Transmission electron microscopy (TEM) images were taken on a Hitachi HT7700 transmission electron microscope with an acceleration voltage of 100 kV. Photocurrent–voltage (J–V) was measured by ZAHNER CIMPS electrochemical workstation, Germany. The forward bias for stability characterization of the solar cell was held to 0.865 V. The active area was fixed at 0.16 cm<sup>2</sup> attached with a mask of 0.09 cm<sup>2</sup>. External quantum efficiency (EQE) spectra were recorded using a computer-controlled setup consisting of a xenon light source, a monochromator, and a potentiostat with wavelength ranging from 370 to 800 nm.

## ASSOCIATED CONTENT

### Supporting Information

The Supporting Information is available free of charge on the ACS Publications website at DOI: 10.1021/jacs.5b06444.

Top–down SEM images of PbI<sub>2</sub>(DMSO)<sub>x</sub> and CH<sub>3</sub>NH<sub>3</sub>PbI<sub>3</sub> thin films prepared by different ratio of DMSO and DMF in CPS; AFM images of perovskite thin film prepared by different ratio of DMSO and DMF in CPS; SEM images of PbI<sub>2</sub>(DMSO)<sub>x</sub> complexes (DMSO-40); photovoltaic performances of perovskite solar cells that were affected by the concentration of MAI and the thickness of TiO<sub>2</sub> mesoporous layer; external quantum efficiency (EQE) spectrum together with EQE date-based integrated J<sub>SC</sub> (PDF)

## AUTHOR INFORMATION

### Corresponding Authors

\*J.F.: jdfan@hbu.edu.cn

\*L.W.: chldwang@mail.tsinghua.edu.cn

### Notes

The authors declare no competing financial interest.

## ACKNOWLEDGMENTS

The research was funded by the National Natural Science Foundation of China (Grant 51273104), “973 Program” Early Projects (Grant 2014CB260405), “Advanced Talents Program of Hebei Province (Grant GCC2014013), Top Young Outstanding Innovative Talents Program of Hebei Province (Grant BJ2014009), and Natural Science Foundation of Hebei Province (Grant F2015201189). J.F. thanks the support of “100 Talents Program of Hebei Province”.

## REFERENCES

- (1) Kojima, A.; Teshima, K.; Shirai, Y.; Miyasaka, T. *J. Am. Chem. Soc.* **2009**, *131*, 6050–6051.
- (2) Burschka, J.; Pellet, N.; Moon, S.-J.; Humphry-Baker, R.; Gao, P.; Nazeeruddin, M. K.; Grätzel, M. *Nature* **2013**, *499*, 316–319.
- (3) Green, M. A.; Ho-Baillie, A.; Snaith, H. J. *Nat. Photonics* **2014**, *8*, 506–514.
- (4) Jeon, N. J.; Noh, J. H.; Yang, W. S.; Kim, Y. C.; Ryu, S.; Seo, J.; Seok, S. I. *Nature* **2015**, *517*, 476–480.
- (5) Kim, H.-S.; Lee, C.-R.; Im, J.-H.; Lee, K.-B.; Moehl, T.; Marchioro, A.; Moon, S.-J.; Humphry-Baker, R.; Yum, J.-H.; Moser, J. E.; Grätzel, M.; Park, N.-G. *Sci. Rep.* **2012**, *2*, 591.
- (6) Lee, M. M.; Teuscher, J.; Miyasaka, T.; Murakami, T. N.; Snaith, H. J. *Science* **2012**, *338*, 643–647.
- (7) Liu, M.; Johnston, M. B.; Snaith, H. J. *Nature* **2013**, *501*, 395–398.
- (8) Mei, A.; Li, X.; Liu, L.; Ku, Z.; Liu, T.; Rong, Y.; Xu, M.; Hu, M.; Chen, J.; Yang, Y.; Grätzel, M.; Han, H. *Science* **2014**, *345*, 295–298.
- (9) Yang, W. S.; Noh, J. H.; Jeon, N. J.; Kim, Y. C.; Ryu, S.; Seo, J.; Seok, S. I. *Science* **2015**, *348*, 1234–1237.
- (10) Fan, J.; Jia, B.; Gu, M. *Photonics Res.* **2014**, *2*, 111–120.
- (11) Zhou, H.; Chen, Q.; Li, G.; Luo, S.; Song, T.-b.; Duan, H.-S.; Hong, Z.; You, J.; Liu, Y.; Yang, Y. *Science* **2014**, *345*, 542–546.
- (12) Stranks, S. D.; Eperon, G. E.; Grancini, G.; Menelaou, C.; Alcocer, M. J. P.; Leijtens, T.; Herz, L. M.; Petrozza, A.; Snaith, H. J. *Science* **2013**, *342*, 341–344.
- (13) Xing, G.; Mathews, N.; Sun, S.; Lim, S. S.; Lam, Y. M.; Grätzel, M.; Mhaisalkar, S.; Sum, T. C. *Science* **2013**, *342*, 344–347.
- (14) Wehrenfennig, C.; Eperon, G. E.; Johnston, M. B.; Snaith, H. J.; Herz, L. M. *Adv. Mater.* **2014**, *26*, 1584–1589.
- (15) Docampo, P.; Ball, J. M.; Darwich, M.; Eperon, G. E.; Snaith, H. J. *Nat. Commun.* **2013**, *4*, 2761.



- (16) You, J.; Hong, Z.; Yang, Y.; Chen, Q.; Cai, M.; Song, T.-B.; Chen, C.-C.; Lu, S.; Liu, Y.; Zhou, H.; Yang, Y. *ACS Nano* **2014**, *8*, 1674–1680.
- (17) Liang, P.-W.; Liao, C.-Y.; Chueh, C.-C.; Zuo, F.; Williams, S. T.; Xin, X.-K.; Lin, J.; Jen, A. K. Y. *Adv. Mater.* **2014**, *26*, 3748–3754.
- (18) Chen, C.-W.; Kang, H.-W.; Hsiao, S.-Y.; Yang, P.-F.; Chiang, K.-M.; Lin, H.-W. *Adv. Mater.* **2014**, *26*, 6647–6652.
- (19) Etgar, L.; Gao, P.; Xue, Z.; Peng, Q.; Chandiran, A. K.; Liu, B.; Nazeeruddin, M. K.; Grätzel, M. *J. Am. Chem. Soc.* **2012**, *134*, 17396–17399.
- (20) Seo, J.; Park, S.; Chan Kim, Y.; Jeon, N. J.; Noh, J. H.; Yoon, S. C.; Seok, S. I. *Energy Environ. Sci.* **2014**, *7*, 2642–2646.
- (21) Chen, Q.; Zhou, H.; Hong, Z.; Luo, S.; Duan, H.-S.; Wang, H.-H.; Liu, Y.; Li, G.; Yang, Y. *J. Am. Chem. Soc.* **2014**, *136*, 622–625.
- (22) Chen, Q.; Zhou, H.; Song, T.-B.; Luo, S.; Hong, Z.; Duan, H.-S.; Dou, L.; Liu, Y.; Yang, Y. *Nano Lett.* **2014**, *14*, 4158–4163.
- (23) Liu, C.; Fan, J.; Zhang, X.; Shen, Y.; Yang, L.; Mai, Y. *ACS Appl. Mater. Interfaces* **2015**, *7*, 9066–9071.
- (24) Knop, O.; Wasylshen, R. E.; White, M. A.; Cameron, T. S.; Oort, M. J. M. V. *Can. J. Chem.* **1990**, *68*, 412–422.
- (25) Liang, K.; Mitzi, D. B.; Prikas, M. T. *Chem. Mater.* **1998**, *10*, 403–411.
- (26) Li, W.; Dong, H.; Dong, H.; Li, J.; Li, W.; Niu, G.; Guo, X.; Wu, Z.; Wang, L. *J. Mater. Chem. A* **2014**, *2*, 14973–14978.
- (27) Li, W.; Dong, H.; Wang, L.; Li, N.; Guo, X.; Li, J.; Qiu, Y. *J. Mater. Chem. A* **2014**, *2*, 13587–13592.
- (28) Wu, Y.; Islam, A.; Yang, X.; Qin, C.; Liu, J.; Zhang, K.; Peng, W.; Han, L. *Energy Environ. Sci.* **2014**, *7*, 2934–2938.
- (29) Rong, Y.; Tang, Z.; Zhao, Y.; Zhong, X.; Venkatesan, S.; Graham, H.; Patton, M.; Jing, Y.; Guloy, A. M.; Yao, Y. *Nanoscale* **2015**, *7*, 10595–10599.
- (30) Ito, S.; Tanaka, S.; Nishino, H. *J. Phys. Chem. Lett.* **2015**, *6*, 881–886.
- (31) Zhang, T.; Yang, M.; Zhao, Y.; Zhu, K. *Nano Lett.* **2015**, *15*, 3959–3963.
- (32) Wakamiya, A.; Endo, M.; Sasamori, T.; Tokito, N.; Ogomi, Y.; Hayase, S.; Murata, Y. *Chem. Lett.* **2014**, *43*, 711–713.
- (33) Selbin, J.; Bull, W. E.; Holmes, L. H., Jr. *J. Inorg. Nucl. Chem.* **1961**, *16*, 219–224.
- (34) Miyamae, H.; Numahata, Y.; Nagata, M. *Chem. Lett.* **1980**, *9*, 663–664.
- (35) Winnik, M. A. *Curr. Opin. Colloid Interface Sci.* **1997**, *2*, 192–199.